

Synthesizing of $(\text{Bi}_2\text{O}_3)_{1-x-y}(\text{Ho}_2\text{O}_3)_x(\text{Dy}_2\text{O}_3)_y$ Electrolytes for Intermediate-Temperature Solid Oxide Fuel Cells

M. KAŞIKCI ÖZEN^a, R. KAYALI^{a,*}, N. ÇIÇEK BEZİR^b AND A. EVCİN^c

^aDepartment of Physics, Science-Literature Faculty, Niğde University, Niğde, Turkey

^bDepartment of Physics, Science-Literature Faculty, Süleyman Demirel University, Isparta, Turkey

^cDepartment of Materials Science and Engineering, Faculty of Engineering, University of Afyon Kocatepe, Afyonkarahisar, Turkey

(Received January 12, 2015; in final form December 7, 2015)

In present study, Ho_2O_3 and Dy_2O_3 doped Bi_2O_3 composite materials for intermediate-temperature solid oxide fuel cells (IT-SOFCs) were investigated. $(\text{Bi}_2\text{O}_3)_{1-x-y}(\text{Ho}_2\text{O}_3)_x(\text{Dy}_2\text{O}_3)_y$ ternary systems ($x = 0.11, 0.13, 0.15$ and $y = 0.01, 0.03, 0.05, 0.07$) were fabricated using conventional solid-state synthesis techniques. The samples were characterized by means of X-ray powder diffraction, scanning electron microscopy, energy dispersive X-ray spectroscopy, differential thermal analysis/thermal gravimeter, and the four-point probe technique. X-ray powder diffraction measurements indicated that all samples have the stable fluorite type face centered cubic (fcc) $\delta\text{-Bi}_2\text{O}_3$ phase. Scanning electron microscopy micrographs of all of the samples showed that grain size distribution was uniform. Four-point probe technique measurements showed that the conductivity of the samples increase with increase of temperature. Additionally, it has been found that the maximum conductivity values of all samples fall in a range 8.44×10^{-2} – $4.60 \times 10^{-1} \text{ S cm}^{-1}$ and their conductivity values corresponding to the intermediate-temperature region vary in the range 1.65×10^{-3} – $2.30 \times 10^{-1} \text{ S cm}^{-1}$. The activation energy values of the samples were calculated from $\log \sigma$ graphics versus $1000/T$ using the Arrhenius equation. It was found that there is a good agreement between the activation energy values and conductivity values.

DOI: [10.12693/APhysPolA.129.125](https://doi.org/10.12693/APhysPolA.129.125)

PACS: 82.47.Ed

1. Introduction

In recent years, fuel cells are attracting tremendous interest because of their direct conversion ability of the electrochemical energy stored in fuel into electrical energy, low system cost, very low pollutants, and great potential for power-generation to meet the demand of various applications with high efficiency. There are many types of the fuel cells and they are, generally, classified according to the electrolyte types used [1], such as phosphoric acid fuel cell (PAFC), proton exchange membrane (PEM) fuel cell, molten carbonate fuel cell (MCFC), direct methanol fuel cell (DMFC), alkaline fuel cell (AFC) and solid oxide fuel cell (SOFC) [2–6] in which solid oxide ceramic electrolytes are used [7–10].

Electrolytes are known as the heart of the SOFC's and the first conventional solid oxide ceramic electrolytes are yttrium doped stabilized zirconium based electrolytes and there are many researchers who have been already studying on different doped zirconia-based electrolytes [11–13]. Yttrium stabilized zirconia-based (YSZ) electrolytes have high ionic conductivity ($\approx 0.1 \text{ S cm}^{-1}$) at temperature range (800–1000 °C) [14] and similar conductivity values have been obtained for Mg doping instead of Y, but it is achieved at very high temperature range (1300–1500 °C) [15]. The high temperature

contributes to an increase in conductivity, on the other hand, it leads to many difficulties, such as corrosion of the metallic components, a decrease in the performance of SOFC and expansion of the component materials causing matching problems [16]. Thus many researchers have focused on developing the electrolytes operating at lower temperature ranges (600–800 °C). This temperature range is called intermediate temperature range (IT) and the solid oxide fuel cells operating in this temperature range are named the intermediate temperature solid oxide fuel cells (IT-SOFCs). Most of the electrolytes studied by the researchers so far are the bismuth-based electrolytes since they have superb ionic conductivity ($\approx 0.1 \text{ S cm}^{-1}$) at IT range [17–19]. Additionally, these bismuth-based electrolytes show that they have high conductivity rapid start-up, but not have better stability, improved durability and higher robustness compared to zirconium-based electrolytes [19–21]. These studies, especially, have been concentrated on bismuth-based binary [22–24] and ternary type ceramic electrolytes [17, 25–28] to improve their conductivity, stability and durability. Researchers studying the binary system electrolytes have observed that nearly all of them have the stable cubic $\delta\text{-Bi}_2\text{O}_3$ phase and their conductivities vary from $\approx 10^{-7}$ to $\approx 10^{-2} \text{ S cm}^{-1}$ [20, 29]. The stable cubic $\delta\text{-Bi}_2\text{O}_3$ phase is also dominant for the ternary system electrolytes and the only difference is about the conductivity values which are varying from ≈ 0.01 to $\approx 0.1 \text{ S cm}^{-1}$ [16, 27, 30, 31].

There are studies on doping to BiYO ternary systems in the literature and the highest conductivity achieved

*corresponding author; e-mail: refikkayali@nigde.edu.tr

was 0.5 S cm^{-1} for Zr doping [32]. However α , β , γ and δ phases of Bi_2O_3 are extensively studied by Norberg et al. [33]. The other research group have made a similar study on α , β , γ and δ -phases of Bi_2O_3 for IT-SOFC's and high ionic conductivity and stabilized δ -phase was achieved by TiO_2 doping [24]. The δ - Bi_2O_3 phase exhibits the highest oxygen conductivity among all bismuth oxide phases in IT-SOFC's [34, 35]. The stable δ -phase of Bi_2O_3 is obtained only in the temperature range of $730\text{--}825^\circ\text{C}$ and exhibit lower conductivity at temperatures below 730°C [36–38]. Therefore, in order to obtain the electrolytes with high ionic conductivity properties and stable fluoride type face-centered cubic (fcc) δ - Bi_2O_3 phase at IT region, researchers have investigated doping Bi_2O_3 by MO_x ($M = \text{Ho, Dy, Er, Tb, Tm, Eu, Ce, etc.}$) type oxides and as a result ternary systems [28, 39–43] or binary systems [44–48] were obtained. The conclusion drawn from these studies is the conductivities of the ternary system electrolytes are higher than binary system electrolytes.

In present study, we fabricated $(\text{Bi}_2\text{O}_3)_{1-x-y}(\text{Ho}_2\text{O}_3)_x(\text{Dy}_2\text{O}_3)_y$ ternary systems ($x = 0.11, 0.13, 0.15$ and $y = 0.01, 0.03, 0.05, 0.07$) having the stable fluoride type face-centered cubic (fcc) δ - Bi_2O_3 phase that can be used as an electrolyte material in the IT-SOFC's by the SST method. The fabricated samples were characterized by X-ray powder diffraction (XRD), scanning electron microscopy (SEM), energy dispersive X-ray spectroscopy (EDX), differential thermal analysis (DTA), thermal gravimetry analysis (TGA), and the four-point probe technique (FPPT) in order to examine their morphological, structural, thermal and electrical properties.

2. Experimental procedures

2.1. Sample preparations

We produced three different group samples $(\text{Bi}_2\text{O}_3)_{1-x-y}(\text{Ho}_2\text{O}_3)_x(\text{Dy}_2\text{O}_3)_y$ ternary system, naming as group A (A1, A2, A3, A4, for $x = 11$ and $y = 1, 3, 5, 7$), group B (B1, B2, B3, B4, for $x = 13$ and $y = 1, 3, 5, 7$), and group C (C1, C2, C3, C4, for $x = 15$ and $y = 1, 3, 5, 7$) by SST using the appropriate amounts of holmium (+3) oxide (Ho_2O_3 , purity 99.99%, Alfa Aesar), dysprosium (+3) oxide (Dy_2O_3 , purity 99.99%, Alfa Aesar) and bismuth (+3) oxide (Bi_2O_3 , purity 99.99%, Alfa Aesar).

The flow chart showing the experimental steps to fabricate the samples and their preparations for the measurements is given in Fig. 1.

The desired proportion of each of the ceramic materials was accurately weighed out in stoichiometric quantities and then they were homogeneously mixed by grinding in an agate mortar. Each of the powder mixtures was synthesized in a ceramic crucible at 750°C for 48 h to obtain stable fluorite type face centered cubic (fcc) δ - Bi_2O_3 phase and by this way 12 different powder mixtures were prepared.

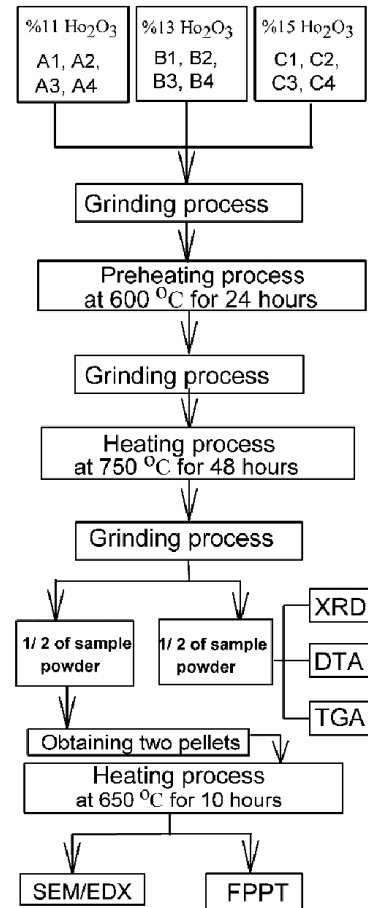


Fig. 1. Experimental flow chart of $(\text{Bi}_2\text{O}_3)_{1-x-y}(\text{Ho}_2\text{O}_3)_x(\text{Dy}_2\text{O}_3)_y$ ternary system samples.

The prepared powder of each sample, first, was divided into two parts. One part was employed to obtain pellets with a diameter of 10 mm and thickness of 2 mm by applying 10 MPa then these pellets were sintered at 650°C for 10 h. These pellets were used for SEM, EDX, and FPPT measurements. The other part was left in powder form for XRD, DTA, and TGA measurements.

2.2. X-ray diffraction analyses

XRD powder diffraction measurements were performed for the determination of the crystal phases of the samples, using a Shimadzu XRD-6000, equipped with a copper X-ray source ($\lambda = 1.544 \text{ \AA}$), and a monochromatic eliminating K_β radiation. During the measurements, the scanning was carried out from 20° to 80° with a step of $0.002^\circ/\text{min}$. The unit cell parameters and crystalline phases of the samples were determined by Match software.

2.3. Microstructural studies

The surface morphology and microstructure of samples were determined by SEM using a LEO 1430 VP. The samples were coated by gold ahead of the SEM measurements. The local composition of grains were determined via EDX that is attached to the SEM.

2.4. Thermal analyses

Thermal analysis (DTA/TG) of the samples was studied by using a NETZSCH model device, in the temperature range of 25–800 °C with 0.001–30 K/min heating rate.

2.5. Electrical measurements

The electrical conductivity measurements of the samples in the form of the pellet were performed by means of our home made FPPT system. All of the electrical measurements were determined by using Data Acquisition Control System integrated with a PC, interface card IEEE-488.2, multi meter with scanning card (Keithley 2700, 7700-2), programmable power supply (Keithley 2400), and computer program written for this purpose. The obtained data was used to plot the Arrhenius conductivity.

3. Results and discussion

3.1. XRD measurement results

Figure 2 shows the XRD patterns of the powder samples with varying holmium oxide and dysprosium oxide contents. As seen from Fig. 2, all $(\text{Bi}_2\text{O}_3)_{1-x-y}(\text{Ho}_2\text{O}_3)_x(\text{Dy}_2\text{O}_3)_y$ samples have a stable fluorite type face centered cubic (fcc) δ - Bi_2O_3 phase in a wide stoichiometric doping range. As a result, we can say that these different doping ratios of the dopants do not change the stable cubic δ - Bi_2O_3 phase of the samples. In the present study, we investigated only the samples sintered at 750 °C for 48 h, since the highest ionic conductivity was obtained at this sintering temperature in our previous similar research [49].

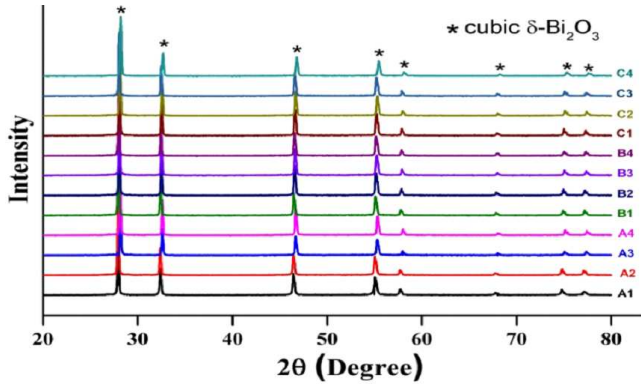


Fig. 2. XRD patterns of the $(\text{Bi}_2\text{O}_3)_{1-x-y}(\text{Ho}_2\text{O}_3)_x(\text{Dy}_2\text{O}_3)_y$ ternary system samples sintered at 750 °C for 48 h.

Figure 3 shows the variation of the lattice parameter, a , depending on the amount of Dy_2O_3 doped A, B, and C group $(\text{Bi}_2\text{O}_3)_{1-x-y}(\text{Ho}_2\text{O}_3)_x(\text{Dy}_2\text{O}_3)_y$ ternary system samples. As can be seen in Fig. 3, the lattice parameters of all samples decrease with increasing Dy_2O_3 content. The lattice parameter, a , values of the samples

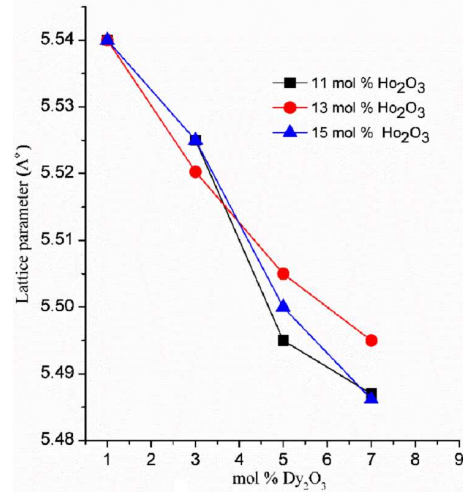


Fig. 3. Variation of the lattice parameter, a , of A, B, and C group samples as a function of Dy_2O_3 amount.

obtained from XRD measurements are given in Table I and they are in the range 5.5400–5.4862 Å. These results are in a good agreement with the results obtained from similar studies in literature [7, 24, 25].

The decrease in lattice parameters of the samples (A, B and C groups) may be attributed to the difference between the ionic radii of Bi^{+3} and Dy^{+3} . The ionic radius of Dy^{+3} (105.2 pm) is smaller compared to the ionic radius of Bi^{+3} (117.0 pm). Therefore, a decrease is expected in lattice parameters of the samples with the increasing amount of Dy^{+3} [8].

3.2. Electrical conductivity measurements

We have carried out FPPT for the conductivity measurements for solid electrolytes and all conductivity measurements of the samples were performed within the temperature range of 150–910 °C. Figure 4a–c shows the temperature dependence of electrical conductivities of the A, B, and C group samples, respectively. All conductivity curves show the typical characteristic of solid ceramic materials and obey the Arrhenius equation. Conductivity values corresponding to different temperatures were determined directly from curves and their activation energy values have been calculated from their $\log \sigma$ graphics using the Arrhenius equation

$$\sigma = \sigma_0 \exp\left(-\frac{E_a}{k_B T}\right), \quad (1)$$

where σ_0 is the conductivity, E_a is the activation energy of the O^{2-} ions, T is the temperature in K, k_B is the Boltzmann constant having value 1.38×10^{-23} J/K. We calculated the activation energies of all samples using a part of their conductivity curves with a constant slope and corresponding to the IT-region (T_1 – T_2). The obtained conductivity values of the samples from their conductivity curves are given in Fig. 4 and their calculated activation energy values samples have been given in Table I.

TABLE I

Doping amount of (Bi_2O_3), (Ho_2O_3), (Dy_2O_3), electrical conductivity, activation energies and lattice parameters of the samples annealed at 750°C for 48 h.

Samples	Ho_2O_3 (x) [mol%]	Dy_2O_3 (y) [mol%]	σ_{max} [S cm^{-1}]	T_{max} [$^\circ\text{C}$]	σ_1 [S cm^{-1}]	σ_2 [S cm^{-1}]	T_1 [$^\circ\text{C}$]	T_2 [$^\circ\text{C}$]	E_a [eV]	Lattice parameter [\AA]
A1	11	1	1.51×10^{-1}	784	1.18×10^{-2}	1.51×10^{-1}	580	784	0.97	5.5400
A2	11	3	4.60×10^{-1}	910	2.74×10^{-3}	1.80×10^{-2}	567	765	0.71	5.5250
A3	11	5	4.42×10^{-1}	882	4.05×10^{-2}	1.14×10^{-1}	672	766	0.93	5.4950
A4	11	7	2.30×10^{-1}	880	2.29×10^{-3}	9.12×10^{-2}	516	785	0.98	5.4870
B1	13	1	2.37×10^{-1}	791	1.65×10^{-3}	5.86×10^{-2}	492	785	0.85	5.5400
B2	13	3	1.27×10^{-1}	868	4.46×10^{-3}	2.88×10^{-2}	562	715	0.86	5.5203
B3	13	5	1.50×10^{-1}	843	5.21×10^{-3}	2.45×10^{-2}	652	776	0.74	5.5050
B4	13	7	1.83×10^{-1}	855	3.98×10^{-3}	1.97×10^{-2}	608	784	0.73	5.4995
C1	15	1	8.44×10^{-2}	871	8.6×10^{-3}	2.82×10^{-2}	667	797	0.79	5.5400
C2	15	3	2.91×10^{-1}	869	1.85×10^{-3}	1.76×10^{-2}	585	765	0.96	5.5250
C3	15	5	1.83×10^{-1}	784	1.13×10^{-2}	7.07×10^{-2}	620	770	0.98	5.5000
C4	15	7	1.37×10^{-1}	829	3.86×10^{-3}	1.11×10^{-1}	541	783	1.02	5.4862

As seen from Fig. 4a, all curves have similar characteristics as expected for solid ceramic materials. Nearly all samples begin to become conductive around 300°C and their conductivities increase abruptly above this temperature. This is an expected result because the number of the free O^{2-} ion vacancies increases with increasing temperature resulting in an increase in the conductivity of the ceramic materials [50]. As seen from Table I, the samples in group A have the maximum conductivity values corresponding to different T_{max} temperatures (A_1 : $1.51 \times 10^{-1} \text{ S cm}^{-1}$ at 784°C , A_2 : $4.60 \times 10^{-1} \text{ S cm}^{-1}$ at 910°C , A_3 : $4.42 \times 10^{-1} \text{ S cm}^{-1}$ at 882°C , A_4 : $2.30 \times 10^{-1} \text{ S cm}^{-1}$ at 880°C). Also, the conductivity values of these samples (σ_1 and σ_2) corresponding to the beginning and end of the IT region are close to these maximum conductivity values. The calculated activation energies of A_1 , A_2 , A_3 , and A_4 samples belonging to IT-region are 0.97, 0.71, 0.93, and 0.98 eV, respectively. As seen in Table I, there is a good agreement between the activation energies and the conductivity values of these samples. Because, the conductivities of all samples increase with decrease in activation energy. It is well known that O^{2-} ion vacancies increase with the temperature when a ceramic material has a small activation energy [50]. Hence the flow of the O^{2-} ions will increase resulting in an increase in the conductivity.

Figure 4b and c shows $\log \sigma$ versus $1000/T$ curves of $(\text{Bi}_2\text{O}_3)_{1-x-y}(\text{Ho}_2\text{O}_3)_x(\text{Dy}_2\text{O}_3)_y$ ternary systems ($x = 0.13$ and $y = 0.01, 0.03, 0.05, 0.07$) and ($x = 0.15$ and $y = 0.01, 0.03, 0.05, 0.07$), respectively. The conductivity curves of these samples show similar behaviors as group A samples. As seen from Table I, all B and C group samples have the maximum conductivity values corresponding to different T_{max} temperatures (B_1 : $2.37 \times 10^{-1} \text{ S cm}^{-1}$ at 791°C , B_2 : $1.27 \times 10^{-1} \text{ S cm}^{-1}$ at 868°C , B_3 : $1.50 \times 10^{-1} \text{ S cm}^{-1}$ at 843°C , B_4 : $1.83 \times 10^{-1} \text{ S cm}^{-1}$

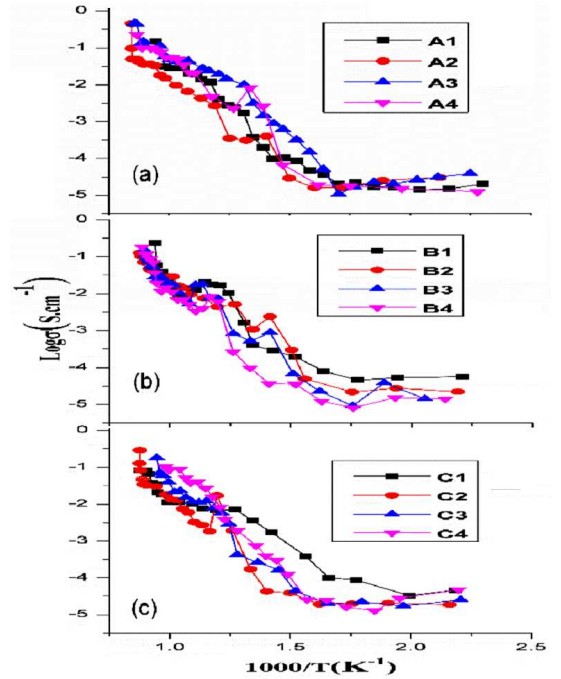


Fig. 4. The temperature dependence of electrical conductivities of the $(\text{Bi}_2\text{O}_3)_{1-x-y}(\text{Ho}_2\text{O}_3)_x(\text{Dy}_2\text{O}_3)_y$ samples ($y = 0.01, 0.03, 0.05, 0.07$) developed at 750°C for 48 h for (a) A group ($x = 0.11$), (b) B group ($x = 0.13$), and (c) C group ($x = 0.15$).

at 855°C and C_1 : $8.44 \times 10^{-2} \text{ S cm}^{-1}$ at 871°C , C_2 : $2.91 \times 10^{-1} \text{ S cm}^{-1}$ at 869°C , C_3 : $1.83 \times 10^{-1} \text{ S cm}^{-1}$ at 784°C , C_4 : $1.37 \times 10^{-1} \text{ S cm}^{-1}$ at 829°C). And also, the conductivity values of these samples (σ_1 and σ_2) corresponding to the beginning and end of the IT region are close to these maximum conductivity values as in A group samples. The activation energies of B_1, B_2, B_3, B_4 and C_1, C_2, C_3, C_4 are 0.85, 0.86, 0.74, 0.73 and 0.79, 0.96,

0.98, 1.02 eV, respectively. All these obtained conductivity and activation energy values of the samples are in a good agreement with the results obtained from similar studies in literature [17, 28, 40].

3.3. SEM measurement results

Figure 5 shows SEM images of A group samples of $(\text{Bi}_2\text{O}_3)_{1-x-y}(\text{Ho}_2\text{O}_3)_x(\text{Dy}_2\text{O}_3)_y$ ternary systems (A1, A2, A3, and A4). As seen from Fig. 1, A1 sample has a very porous structure compared the other samples and there is no homogeneity in the grain sizes. Grain size in A2 and A3 samples become larger with increasing Dy_2O_3 and decreasing Bi_2O_3 amount. The shapes of the grains also become smoother compared A1 sample. When A4 is compared to other samples, the grain size in the A4 is larger than A1 and smaller than A2 and A3. It is not observed any porosity in A2, A3 and A4. If we compare the electrical conductivity of A1 sample with the other samples it is seen that its conductivity is smaller than A2, A3, and A4 samples. This result can be attributed to the smoothness of the surfaces of these samples and a bit to the amount of the Dy_2O_3 .

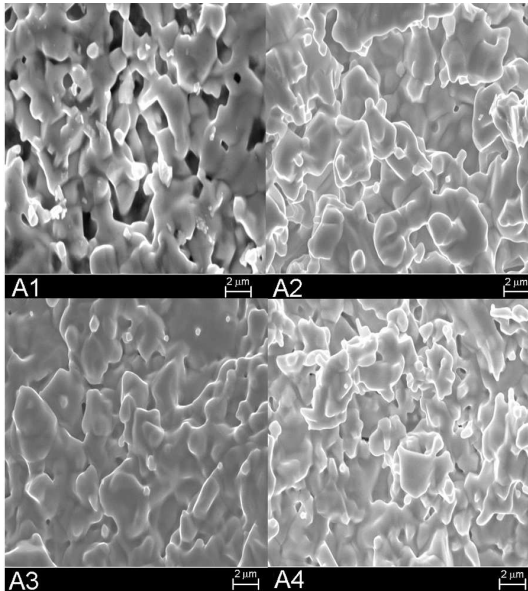


Fig. 5. SEM images of $(\text{Bi}_2\text{O}_3)_{1-x-y}(\text{Ho}_2\text{O}_3)_x(\text{Dy}_2\text{O}_3)_y$ ternary systems A1 ($x = 0.114$, $y = 0.01$), A2 ($x = 0.11$, $y = 0.03$), A3 ($x = 0.11$, $y = 0.05$), and A4 ($x = 0.11$, $y = 0.07$).

Figure 6 shows SEM images of B group samples of $(\text{Bi}_2\text{O}_3)_{1-x-y}(\text{Ho}_2\text{O}_3)_x(\text{Dy}_2\text{O}_3)_y$ ternary systems B1, B2, B3, and B4. As seen from the figure, sample B1 has large sized grains, no pore, a rather smooth surface, and has the highest conductivity compared to other samples. On the other hand, while the grain sizes of the samples B2, B3, and B4 decrease alternately, conversely to this the conductivities of these samples increase. This can be explained with the increase of the amount of Dy_2O_3 and a little bit with the size of the grains and

porosity of the samples. As seen from Fig. 6, the sizes of the grains in B3 and B4 samples are smaller compared B1 and B2 samples and also B3 and B4 samples have much more porosity structure. As a result we can say that porosity plays an important role on the conductivity of the samples to decrease.

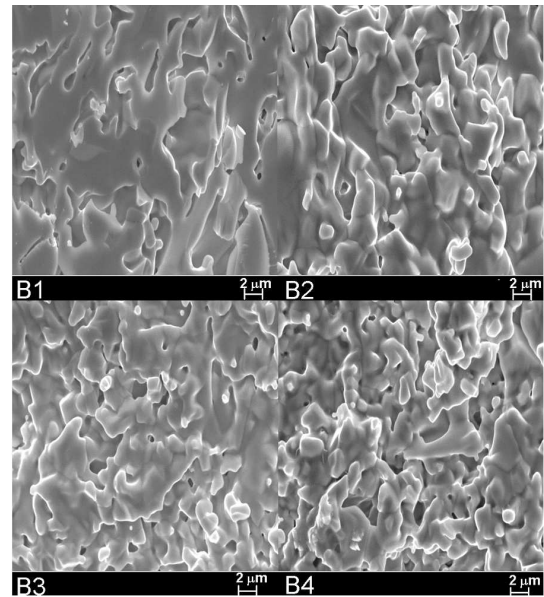


Fig. 6. SEM images of $(\text{Bi}_2\text{O}_3)_{1-x-y}(\text{Ho}_2\text{O}_3)_x(\text{Dy}_2\text{O}_3)_y$ ternary systems B1 ($x = 0.13$, $y = 0.01$), B2 ($x = 0.13$, $y = 0.03$), B3 ($x = 0.13$, $y = 0.05$), and B4 ($x = 0.13$, $y = 0.07$).

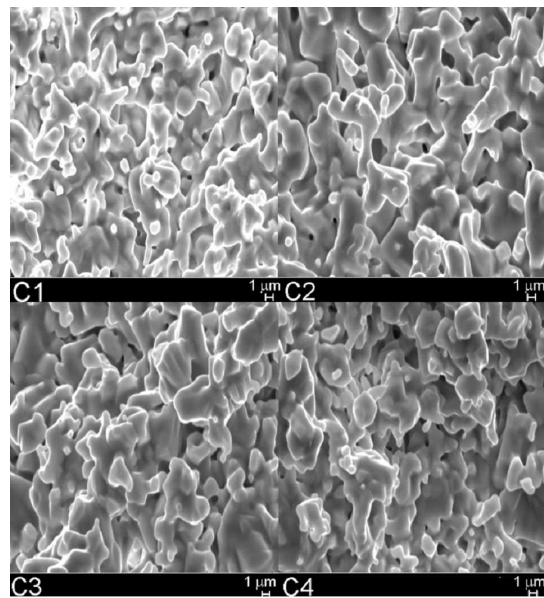


Fig. 7. SEM images of $(\text{Bi}_2\text{O}_3)_{1-x-y}(\text{Ho}_2\text{O}_3)_x(\text{Dy}_2\text{O}_3)_y$ ternary systems C1 ($x = 0.15$, $y = 0.01$), C2 ($x = 0.15$, $y = 0.03$), C3 ($x = 0.15$, $y = 0.05$), and C4 ($x = 0.11$, $y = 0.07$).

Figure 7 shows SEM images of C group samples of $(\text{Bi}_2\text{O}_3)_{1-x-y}(\text{Ho}_2\text{O}_3)_x(\text{Dy}_2\text{O}_3)_y$ ternary systems

C1, C2, C3, and C4. As seen from this figure, the sizes of the grains in samples C4, C2, and C3 are greater than each other, respectively. These samples have rather homogeneous distribution of grains and also less porosity. However, C1 has the smallest grain sizes and much more pores compared to the other samples. When the conductivity of the samples has been compared, it is seen that the conductivity of the samples increase with increasing grain sizes of the samples and also this increase depends on the distributions of the grains and the porosity of the samples. Under the light of these results, we can say that it is the expected result that the conductivities of the samples C1, C4, C2, and C3 must be arranged as being smaller than each other, respectively.

3.4. EDX measurement results

Chemical compositions of the samples were obtained by EDX measurements. The nominal chemical compositions of the as-prepared samples and resulting compositions from EDX microanalysis of $(\text{Bi}_2\text{O}_3)_{1-x-y}(\text{Ho}_2\text{O}_3)_x(\text{Dy}_2\text{O}_3)_y$ ternary systems were given in Table II. It can be seen that there are very small differences between the chemical compositions of the as-prepared samples and the heat treated samples. Therefore, starting and resulting compositions can be accepted as similar and the small differences are attributed to the experimental errors. Also these small differences can be attributed to the experimental errors.

TABLE II

Nominal chemical compositions of the as-prepared samples and resulting compositions from EDX microanalysis of $(\text{Bi}_2\text{O}_3)_{1-x-y}(\text{Ho}_2\text{O}_3)_x(\text{Dy}_2\text{O}_3)_y$ ternary systems developed at 750 °C for 48 h.

Samples	Nominal chemical composition	Resulting composition (EDX analysis)
A1	$(\text{Bi}_2\text{O}_3)_{0.88}(\text{Ho}_2\text{O}_3)_{0.11}(\text{Dy}_2\text{O}_3)_{0.01}$	$(\text{Bi}_2\text{O}_3)_{0.86}(\text{Ho}_2\text{O}_3)_{0.11}(\text{Dy}_2\text{O}_3)_{0.03}$
A2	$(\text{Bi}_2\text{O}_3)_{0.86}(\text{Ho}_2\text{O}_3)_{0.11}(\text{Dy}_2\text{O}_3)_{0.03}$	$(\text{Bi}_2\text{O}_3)_{0.87}(\text{Ho}_2\text{O}_3)_{0.11}(\text{Dy}_2\text{O}_3)_{0.02}$
A3	$(\text{Bi}_2\text{O}_3)_{0.84}(\text{Ho}_2\text{O}_3)_{0.11}(\text{Dy}_2\text{O}_3)_{0.05}$	$(\text{Bi}_2\text{O}_3)_{0.85}(\text{Ho}_2\text{O}_3)_{0.11}(\text{Dy}_2\text{O}_3)_{0.04}$
A4	$(\text{Bi}_2\text{O}_3)_{0.82}(\text{Ho}_2\text{O}_3)_{0.11}(\text{Dy}_2\text{O}_3)_{0.07}$	$(\text{Bi}_2\text{O}_3)_{0.82}(\text{Ho}_2\text{O}_3)_{0.14}(\text{Dy}_2\text{O}_3)_{0.04}$
B1	$(\text{Bi}_2\text{O}_3)_{0.86}(\text{Ho}_2\text{O}_3)_{0.13}(\text{Dy}_2\text{O}_3)_{0.01}$	$(\text{Bi}_2\text{O}_3)_{0.88}(\text{Ho}_2\text{O}_3)_{0.10}(\text{Dy}_2\text{O}_3)_{0.02}$
B2	$(\text{Bi}_2\text{O}_3)_{0.84}(\text{Ho}_2\text{O}_3)_{0.13}(\text{Dy}_2\text{O}_3)_{0.03}$	$(\text{Bi}_2\text{O}_3)_{0.88}(\text{Ho}_2\text{O}_3)_{0.11}(\text{Dy}_2\text{O}_3)_{0.01}$
B3	$(\text{Bi}_2\text{O}_3)_{0.82}(\text{Ho}_2\text{O}_3)_{0.13}(\text{Dy}_2\text{O}_3)_{0.05}$	$(\text{Bi}_2\text{O}_3)_{0.83}(\text{Ho}_2\text{O}_3)_{0.14}(\text{Dy}_2\text{O}_3)_{0.03}$
B4	$(\text{Bi}_2\text{O}_3)_{0.80}(\text{Ho}_2\text{O}_3)_{0.13}(\text{Dy}_2\text{O}_3)_{0.07}$	$(\text{Bi}_2\text{O}_3)_{0.81}(\text{Ho}_2\text{O}_3)_{0.12}(\text{Dy}_2\text{O}_3)_{0.07}$
C1	$(\text{Bi}_2\text{O}_3)_{0.84}(\text{Ho}_2\text{O}_3)_{0.15}(\text{Dy}_2\text{O}_3)_{0.01}$	$(\text{Bi}_2\text{O}_3)_{0.83}(\text{Ho}_2\text{O}_3)_{0.16}(\text{Dy}_2\text{O}_3)_{0.01}$
C2	$(\text{Bi}_2\text{O}_3)_{0.82}(\text{Ho}_2\text{O}_3)_{0.15}(\text{Dy}_2\text{O}_3)_{0.03}$	$(\text{Bi}_2\text{O}_3)_{0.82}(\text{Ho}_2\text{O}_3)_{0.16}(\text{Dy}_2\text{O}_3)_{0.02}$
C3	$(\text{Bi}_2\text{O}_3)_{0.80}(\text{Ho}_2\text{O}_3)_{0.15}(\text{Dy}_2\text{O}_3)_{0.05}$	$(\text{Bi}_2\text{O}_3)_{0.82}(\text{Ho}_2\text{O}_3)_{0.15}(\text{Dy}_2\text{O}_3)_{0.03}$
C4	$(\text{Bi}_2\text{O}_3)_{0.78}(\text{Ho}_2\text{O}_3)_{0.15}(\text{Dy}_2\text{O}_3)_{0.07}$	$(\text{Bi}_2\text{O}_3)_{0.80}(\text{Ho}_2\text{O}_3)_{0.14}(\text{Dy}_2\text{O}_3)_{0.06}$

3.5. Thermal analysis

Comparison of DTA and electrical conductivity curves of the A1, B1, and C1 samples synthesized at 750 °C for 48 h are given in Fig. 8a–c, respectively. As seen from Fig. 8a, the first peak appearing at 315 °C on the DTA curve indicates an exothermic reaction. At this temperature there is a transition from monoclinic α -phase to tetragonal β -phase according to the conductivity curve. Around 404 °C, thermogram of this composition shows a weak endothermic reaction implying that the sample has tetragonal β -phase. However, at 469 °C a strong endothermic reaction appears. It means that there is an order/disorder transformation in the structure rather than the phase transformation and this result is confirmed by comparing the conductivity curves. At 557 °C a strong exothermic reaction is observed. When we take a look at conductivity curve of the sample, it is seen that the sample has a mixed $(\beta + \delta)$ -phase at this temperature. This temperature can be assumed as a

critical point for transition from β -phase to mixed $(\beta + \delta)$ -phase. At 625 °C, a very strong endothermic reaction is observed. At this temperature, the mixed $(\beta + \delta)$ -phase completely transforms into δ -phase since that can be understood by rapid increase in the conductivity above this temperature [49]. By comparing the DTA and electrical conductivity curves in Fig. 8b and c it is observed that all events occurring in these samples are nearly similar that differs from the first sample. The same phase transitions in these two samples are seen at the same temperatures as the first sample.

Comparison of DTA and TGA curves of A1, B1, and C1 samples synthesized at 750 °C for 48 h are given in Fig. 9a–c, respectively. As seen from this figure, the mass losses in all samples happen until approximately 470 °C, but after this temperature it has been seen that there is no mass loss for all samples depending on the exothermic and endothermic reactions.

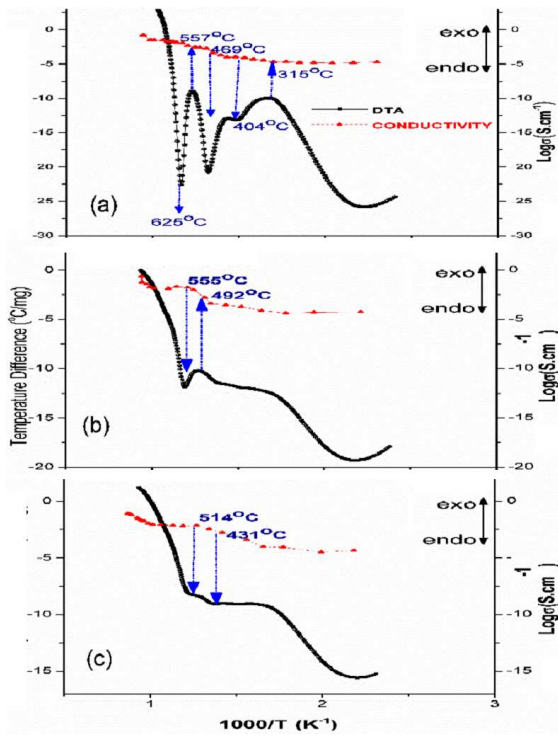


Fig. 8. Arrhenius plot of conductivity and DTA curves for the $(\text{Bi}_2\text{O}_3)_{1-x-y}(\text{Ho}_2\text{O}_3)_x(\text{Dy}_2\text{O}_3)_y$ samples (a) A1 ($x = 0.11$, $y = 0.01$), (b) B1 ($x = 0.13$, $y = 0.01$), and (c) C1 ($x = 0.15$, $y = 0.01$) synthesized at 750°C for 48 h.

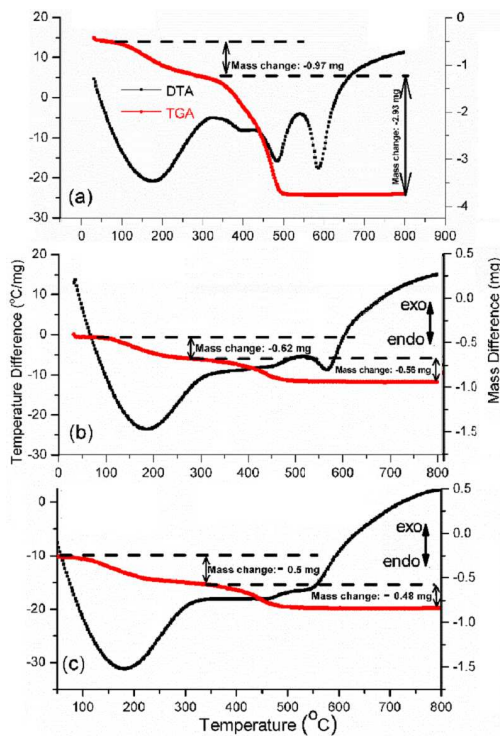


Fig. 9. TGA and DTA curves for the $(\text{Bi}_2\text{O}_3)_{1-x-y}(\text{Ho}_2\text{O}_3)_x(\text{Dy}_2\text{O}_3)_y$ samples (a) A1 ($x = 0.11$, $y = 0.01$), (b) B1 ($x = 0.13$, $y = 0.01$), and (c) C1 ($x = 0.15$, $y = 0.01$) synthesized at 750°C for 48 h.

4. Conclusion

In this work, $(\text{Bi}_2\text{O}_3)_{1-x-y}(\text{Ho}_2\text{O}_3)_x(\text{Dy}_2\text{O}_3)_y$ ($x = 0.11, 0.13, 0.15$ and $y = 0.01, 0.03, 0.05, 0.07$) ternary system materials were synthesized by the SST and their structural, morphological, electrical, and chemical properties were investigated in detail using the data obtained from XRD, EDX, SEM, FPPT, DTA, and TGA experimental measurements. According to the XRD results all the samples have completely homogeneous fluorite type fcc $\delta\text{-Bi}_2\text{O}_3$ phase. It was also observed that the lattice parameters, a , of all samples decrease while the amount of Dy_2O_3 doping materials increases. This decrease in lattice parameter, a , was attributed to the difference in ionic radii of Bi^{+3} and Dy^{+3} cations as Dy^{+3} cations has smaller radius than Bi^{+3} and will replace Bi^{+3} in crystal unit cell. EDX analysis results showed that chemical compositions of all the $(\text{Bi}_2\text{O}_3)_{1-x-y}(\text{Ho}_2\text{O}_3)_x(\text{Dy}_2\text{O}_3)_y$ ternary system samples did not change. The SEM measurements showed that all samples have similar grain sizes and distributions of the grains with an exception for sample B1 since its grain sizes are larger compared to the others. On the other hand, FPPT measurements indicate that conductivities of all samples corresponding the temperatures falling into IT region and have high values varying in the range of $\approx 10^{-3} - 10^{-1} \text{ S cm}^{-1}$. FPPT measurements also showed that the average conductivity values of group A ($\sigma_{\text{Aav}} = 5.27 \times 10^{-1} \text{ S cm}^{-1}$), B ($\sigma_{\text{Bav}} = 1.83 \times 10^{-1} \text{ S cm}^{-1}$), and C ($\sigma_{\text{Cav}} = 3.16 \times 10^{-1} \text{ S cm}^{-1}$) samples are smaller than each other, respectively. In addition, sample A1 ($(\text{Bi}_2\text{O}_3)_{0.86}(\text{Ho}_2\text{O}_3)_{0.11}(\text{Dy}_2\text{O}_3)_{0.03}$) has the highest conductivity value ($\sigma_{\text{A1}} = 1.51 \times 10^{-1} \text{ S cm}^{-1}$) among all samples.

DTA and TGA measurements revealed that there is a good agreement between the chemical reactions (endothermic and exothermic) and the phase transitions and order disorder phenomena.

As a result, all electrolyte samples fabricated by us can be used for IT-SOFC's after their durability and efficiency tests for long period of time.

Acknowledgments

The authors would like to thank TUBITAK, for this study has been supported by TUBITAK with program number BIDEB 2211/C.

References

- [1] J. Huang, F. Xie, C. Wang, Z. Mao, *Int. J. Hydrogen Energy*. **37**, 877 (2012).
- [2] T.F. Cao, H. Lin, L. Chen, Y.L. He, W.Q. Tao, *Appl. Energy*. **112**, 1115 (2013).
- [3] A.M. Zainoodin, S.K. Kamarudin, M.S. Masdar, W.R.W. Daud, A.B. Mohamad, J. Sahari, *Appl. Energy*. **135**, 364 (2014).
- [4] B. Cox, K. Treyer, *J. Power Sources* **275**, 322 (2015).
- [5] J. Milewski, M. Wołowicz, A. Miller, R. Bernat, *Int. J. Hydrogen Energy*. **38**, 565 (2013).

- [6] A.S. Gruzd, E.S. Trofimchuk, N.I. Nikonorova, E.A. Nesterova, I.B. Meshkov, M.O. Gallyamov, A.R. Khokhlov, *Int. J. Hydrogen Energy* **38**, 32 (2013).
- [7] C.L. Gomez, O.D. Rivera, J.C. Medina, P.S. Bermudez, S. Muhl, A. Zeinert, S.E. Rodil, *Solid State Ion.* **255**, 147 (2014).
- [8] D.S. Khaerudini, G. Guan, P.E. Zhang, X. Hao, Y. Kasai, K. Kusakabe, A. Abudula, *J. Alloys Comp.* **589**, 29 (2014).
- [9] H. Rickert, *Angew Chem. Int. Edit.* **17**, 37 (1978).
- [10] J.B. Goodenough, A. Manthiram, M. Paranthaman, Y.S. Zhen, *Mater. Sci. Eng.* **12**, 357 (1992).
- [11] N.M. Sarnrnes, Z. Cai, *Solid State Ion.* **100**, 39 (1997).
- [12] K. Rajeswari, M.B. Suresh, U.S. Hareesh, Y.S. Rao, D. Das, R. Johnson, *Ceram. Int.* **37**, 3557 (2011).
- [13] C. Suci, H. Tikkanen, I. Wærnhus, F. Goga, E. Dorolti, *Ceram. Int.* **38**, 357 (2012).
- [14] H. Kishimoto, K. Yashiro, T. Shimonosono, M.E. Brito, K. Yamaji, T. Horita, H. Yokokawa, J. Mizusaki, *Electrochim. Acta* **82**, 263 (2012).
- [15] S. Yoon, T. Noh, W. Kim, J. Choi, H. Lee, *Ceram. Int.* **39**, 9247 (2013).
- [16] G. Paściak, J. Chmielowiec, S.H. Chan, *Ceram. Int.* **40**, 8969 (2014).
- [17] S. Durmus, V. Corumlu, T. Cifci, I. Ermis, M. Ari, *Ceram. Int.* **39**, 5241 (2013).
- [18] N.A.S. Webster, C.D. Ling, C.L. Raston, F.J. Lincoln, *Solid State Ion.* **178**, 1451 (2007).
- [19] M.Y. Tan, K.B. Tan, Z. Zainal, C.C. Khaw, S.K. Chen, *Ceram. Int.* **38**, 3403 (2012).
- [20] S.E. Lin, W.C.J. Wei, *J. Eur. Ceram. Soc.* **31**, 3081 (2011).
- [21] C.M. Linn, Y.L. Kuo, C.H. Chou, *Ceram. Int.* **39**, 1711 (2013).
- [22] K. Vasundhara, S.N. Achary, S.J. Patwe, A.K. Sahu, N. Manoj, A.K. Tyagi, *J. Alloys Comp.* **596**, 151 (2014).
- [23] S.S. Baek, N. Lee, B.K. Kim, H. Chang, S.J. Song, J.Y. Park, *Int. J. Hydrogen Energy* **37**, 6823 (2012).
- [24] G. Singla, P.K. Jha, J.K. Gill, K. Singh, *Ceram. Int.* **38**, 2065 (2012).
- [25] C.Y. Hsieh, H.S. Wang, K.Z. Fung, *J. Eur. Ceram. Soc.* **31**, 3073 (2011).
- [26] C.Y. Hsieh, K.Z. Fung, *J. Solid State Electron.* **13**, 951 (2009).
- [27] A. Watanabe, M. Sekita, *Solid State Ion.* **176**, 2429 (2005).
- [28] A.B. Centkowska, F. Krok, I. Abrahams, W. Wrobel, *Solid State Ion.* **203**, 22 (2011).
- [29] S. Yilmaz, O. Turkoglu, I. Belenli, *Mater. Chem. Phys.* **112**, 472 (2008).
- [30] X. Liu, H. Fan, J. Shi, G. Dong, Q. Li, *Int. J. Hydrogen Energy* **39**, 7819 (2014).
- [31] V. Gil, J. Tartaj, C. Moure, P. Duran, *J. Eur. Ceram. Soc.* **26**, 3161 (2006).
- [32] S.F. Wang, Y.F. Hsu, W.C. Tsai, H.C. Lu, *J. Power Sources* **218**, 106 (2012).
- [33] S.T. Norberg, S.G. Eriksson, S. Hull, *Solid State Ion.* **192**, 409 (2011).
- [34] N. Jiang, E.D. Wachsman, S.H. Jung, *Solid State Ion.* **150**, 347 (2002).
- [35] M. Leszczynska, M. Holdynski, F. Krok, I. Abrahams, X. Liu, W. Wrobel, *Solid State Ion.* **181**, 796 (2010).
- [36] M. Struzik, X. Liu, I. Abrahams, F. Krok, M. Malys, J.R. Dygas, *Solid State Ion.* **218**, 25 (2012).
- [37] V. Fruth, G. Dobrescu, V. Bratan, C. Hornoiu, S. Preda, C. Andronescu, M. Popa, *J. Eur. Ceram. Soc.* **27**, 4421 (2007).
- [38] J. Molenda, K. Swierczek, W. Zając, *J. Power Sources* **173**, 657 (2007).
- [39] S. Arasteh, A. Maghsoudipour, M. Alizadeh, A. Nemati, *Ceram. Int.* **37**, 3451 (2011).
- [40] T. Chou, L.D. Liu, W.C.J. Wei, *Ceram. Soc.* **31**, 3087 (2011).
- [41] A.A. Yaremchenko, V.V. Kharton, E.N. Naumovich, A.A. Tonoyan, *Mater. Res. Bull.* **35**, 515 (2000).
- [42] S.H. Jung, E.D. Wachsman, N. Jiang, *Ionics* **8**, 210 (2002).
- [43] J. Chmielowiec, G. Paściak, P. Bujło, *Mater. Sci. Poland* **27**, 1251 (2009).
- [44] V. Fruth, A. Ianculescu, D. Berger, S. Preda, G. Voicu, E. Tenea, M. Popa, *J. Eur. Ceram. Soc.* **26**, 3011 (2006).
- [45] R. Li, Q. Zhen, M. Drache, A. Rubbens, E. Claude, V.R. Noëlle, *Solid State Ion.* **198**, 6 (2011).
- [46] S. Nakayama, *Ceram. Int.* **28**, 907 (2002).
- [47] S. Iyyapushpam, P. Chithralekha, D.P. Padiyan, *Physica B* **405**, 712 (2010).
- [48] Y.L. Kuo, L.D. Liu, S.E. Lin, C.H. Chou, W.C.J. Wei, *J. Eur. Ceram. Soc.* **31**, 3119 (2011).
- [49] R. Kayali, M. Kasıkci, S. Durmus, M. Ari, *Fuel Cells* **4**, 1219 (2011).
- [50] W.D. Callister, D.G. Rethwisch, *Materials Science and Engineering*, 8th ed., Wiley, Asia 2011.